Magnetic and Mechanical Anisotropy in a Manganese 2-Methylsuccinate Framework Structure

Wei Li,[a] Phillip T. Barton,[b] M. S. R. N. Kiran,[c] Ryan P. Burwood,[a] U. Ramamurty,[c] and Anthony K. Cheetham*[a]

Abstract: Hybrid inorganic–organic framework materials exhibit unique properties that can be advantageously tuned through choice of the inorganic and organic components and by control of the crystal structure. We present a new hydrothermally prepared 3D hybrid framework, [Mn(2-methylsuccinate)]$_n$ (**1**), comprising alternating 2D manganese oxide sheets and isolated MnO$_6$ octahedra, pillared via *syn, anti–syn* carboxylates. Powder magnetic characterization shows that the compound is a homospin Mn^{II} ferrimagnet below 2.4 K. The easy-axis is revealed by single-crystal magnetic susceptibility studies and a magnetic structure is proposed. Anisotropic elastic moduli and hardness, observed through nanoindentation on differing crystal facets, were correlated with specific structural features. Such measurements of anisotropy are not commonly undertaken, yet allow for a more comprehensive understanding of structure–property relationships.

Keywords: anisotropy · homospin ferrimagnet · manganese · mechanical properties · metal–organic frameworks

Introduction

Hybrid inorganic–organic framework materials have attracted much attention in the last decade due to their interesting magnetic, electronic, and mechanical properties.[1,2] A major goal is to understand the structure–property relationships within these materials and use that knowledge to do materials design and engineering. One strategy to garner understanding is to study the anisotropy in the physical properties of single crystals. However, despite most of these materials being prepared in single-crystal form, there are relatively few anisotropic studies on magnetism, ferroelectricity, and mechanics of these materials.[1d,2–4] Several groups have reported anisotropic magnetic properties of some 2D and 3D frameworks recently, in which it is found that magnetism along different directions can vary considerably.[1d,3] Gao and co-workers published the single-crystal magnetism of a layered manganese azide, [Mn(N$_3$)$_2$(4,4′-bi-1,2,4-triazole)]$_n$,

which shows first-order metamagnetic and spin-flop transitions parallel and perpendicular to the manganese azide layer.[3a] Kurmoo et al. reported the single-crystal study of two 3D frameworks, {[Co$_5$(OH)$_8$(*trans*-1,4-cyclohexanedicarboxylate)]·4H$_2$O}$_n$ and {[Co$_3$(OH)$_2$(*cis*-1,4-cyclohexanedicarboxylate)$_2$(H$_2$O)$_4$]·2H$_2$O}$_n$, which have chained and layered inorganic connectivity respectively. The former exhibits easy-plane magnetism while the later shows very unusual metamagnetic behavior along the easy axis in contrast to normal ferromagnetic-like behavior perpendicular to it.[1d,3b] Chen and co-workers reported the single-crystal magnetism of two 3D manganese frameworks, [Mn$_3$(1,2,3-triazole-4,5-dicarboxylate)$_2$(H$_2$O)$_2$(NH$_3$)$_2$]$_n$ and [Mn$_3$(1,2,3-triazole-4,5-dicarboxylate)$_2$(H$_2$O)$_4$]$_n$, and both of them show unusual multi-step magnetization jumps along differing crystallographic orientations due to the anisotropic competing interactions between the antiferromagnetic couplings.[3c] Some others carried out single-crystal dielectric studies on hybrid framework materials and found significant anisotropy.[4] Xiong, Kobashiya, and their co-workers studied the single-crystal dielectric behavior of a 3D prussian blue analogue framework, [(imidazolium)$_2$KFe(CN)$_6$]$_n$,[4a] and two 3D iso-structural manganese frameworks, {[Mn$_3$(HCOO)$_6$](H$_2$O)(CH$_3$OH)}$_n$ and {[Mn$_3$(HCOO)$_6$](C$_2$H$_5$OH)}$_n$.[4b,c] All of these frameworks exhibit considerably anisotropic dielectric permittivity along differing crystallographic directions.[4a] Recently, we studied the anisotropic mechanical properties of some open and dense hybrid crystals and demonstrated that the elasticity and hardness along differing crystallographic directions can be correlated directly with various aspects of the underlying crystalline structures, such as chemical bonding, organic linker and space packing.[2,5] Particularly in a 3D dense framework, [Ce(C$_2$O$_4$)(HCOO)]$_n$, we found

[a] Dr. W. Li, R. P. Burwood, Prof. A. K. Cheetham
Department of Materials Science and Metallurgy
University of Cambridge
Cambridge CB2 3QZ (UK)
Fax: (+44) 1223-334567
E-mail: akc30@cam.ac.uk

[b] P. T. Barton
Materials Research Laboratory (MRL) and Materials Department
University of California, Santa Barbara
California 93106 (USA)

[c] Dr. M. S. R. N. Kiran, Prof. U. Ramamurty
Department of Materials Engineering
Indian Institute of Science
Bangalore 560012 (India)

Supporting information for this article is available on the WWW under http://dx.doi.org/10.1002/chem.201101251.

that the crystal orientation dominated by inorganic chains is not necessarily stiffer than the orientation constructed by rigid oxalates from the mechanical properties standpoint.[5a] In terms of infinite diverse structural and chemical variability of hybrid frameworks, this opens the possibility of controlling mechanical properties through a crystal engineering approach.[2,5] As far as we are aware, however, there is no report to date of a combined study of magnetic, ferroelectric, or mechanical anisotropy. In the present work we describe a new 3D hybrid framework, [Mn(2-methylsuccinate)]$_n$ (**1**), that displays both anisotropic homospin ferrimagnetism and anisotropic mechanical properties.

Figure 1. The local coordination environments of Mn1, Mn2, Mn3, and 2-methylsuccinate in **1**.

Results and Discussion

Structure of 1: Our single-crystal X-ray diffraction study (Table 1) reveals that compound **1** is a 3D framework containing 2D inorganic manganese oxide honeycomb layers

Table 1. Crystal data and structure refinement for compound **1**.

Compound	**1**
formula	$C_5H_6O_4Mn$
M_r	185.04
crystal system	trigonal
space group	$R\text{-}3$
a [Å]	11.0825(2)
b [Å]	11.0825(2)
c [Å]	29.5902(9)
α [°]	90.00
β [°]	90.00
γ [°]	120.00
V [Å³]	3147.41(12)
Z	18
ρ_{calcd} [g cm^{-3}]	1.757
μ (Mo$_{K\alpha}$) [mm^{-1}]	1.837
$F(000)$	1674
T/K	120
$R1$, $wR2$ [$I > 2\sigma(I)$][a]	0.0480, 0.1382
$R1$, $wR2$ (all data)[a]	0.0536, 0.1423
GOF on F^2	1.052

[a] $R_1 = \Sigma ||F_o| - |F_c|| / \Sigma |F_o|$ and $wR_2 = \{\Sigma[w(F_o^2 - F_c^2)^2] / \Sigma[w(F_o^2)^2]\}^{1/2}$.

and isolated MnO$_6$ octahedra, which is nearly identical to some Mn^{II} and Mg^{II} glutarates.[6] As seen from Figure 1, the asymmetric unit of compound **1** has a 2-methylsuccinate ligand with a disordered methyl group and three crystallographically independent octahedral Mn^{II} ions. Mn1, Mn2, and Mn3 have 1/6, 1/2, and 1/3 multiplicities, respectively. The Mn2 and Mn3 ions are connected by two μ_2-O atoms of two carboxylates from two different 2-methylsuccinates with Mn2-O-Mn3 angles of 97.17 and 99.87° and a nearest Mn2···Mn3 distance of 3.315 Å. The edge-sharing Mn2O$_6$ and Mn3O$_6$ octahedra connect in an alternating mode to form 12-membered rings. Each 12-membered ring is linked to six other rings by sharing six Mn3O$_6$ octahedra to form an infinite two-dimensional honeycomb layer in the *ab* plane (Figure 2a). These layers are cross-linked between Mn2O$_6$
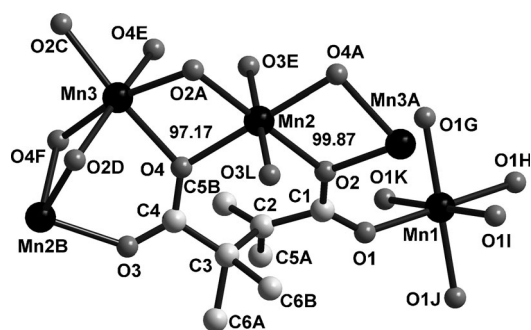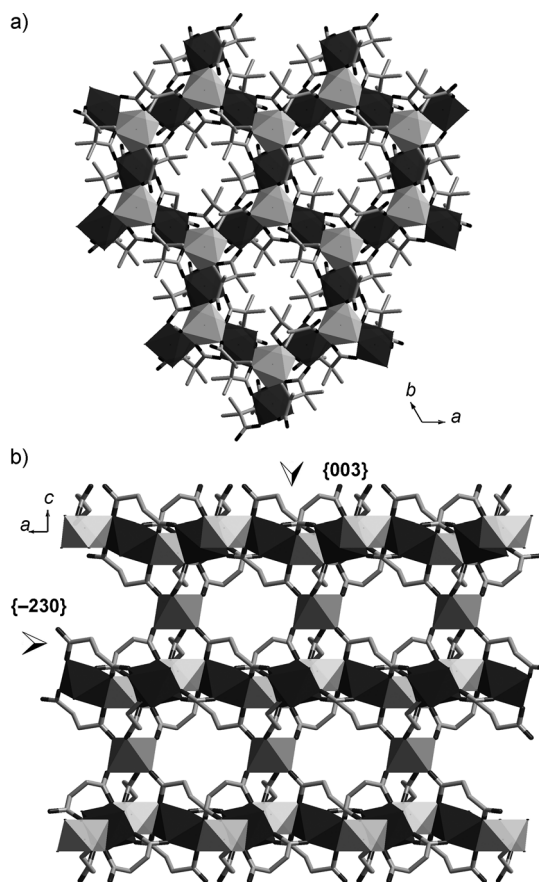

Figure 2. a) Layered structure constructed by edge-sharing 12-membered MnO$_6$ octahedra rings lying in the *ab* plane. b) 3D framework constructed by adjacent layers via isolated Mn1O$_6$ octahedra by *syn, anti–syn* carboxylates lying along the *b* axis (disordered methyl groups are omitted for clarity). Mn1O$_6$, Mn2O$_6$, and Mn3O$_6$ octahedra are presented by grey, black and white respectively.

and Mn3O$_6$ octahedra by isolated Mn1O$_6$ octahedra via *syn, anti–syn* carboxylate linkages[7] to generate a 3D framework (Figure 2b). The nearest distances of Mn3···Mn1 and Mn2···Mn1, 4.065 and 5.879 Å, respectively, are both much longer than the nearest Mn2···Mn3 distance within the 2D inorganic layers. Alternating inorganic manganese oxide

layers are spatially translated by $a/2$ and $b/2$ length along the a- and b axes, which precludes any porosity in the structure.

Thermal analysis of compound 1: Thermogravimetric analysis (TGA) of $[Mn(C_5H_4O_4)]_n$ was carried from 25 to 800 °C in air. As shown in Figure S6 in the Supporting Information, there is no significant mass loss below 295 °C, the temperature at which the compound decomposes. Then the compound suffers complete decomposition until it reaches a temperature of 450 °C, the total mass loss of 57.8 % corresponding to the complete decomposition of the ligand (calcd: 57.3 wt %). This is consistent with the crystal structure and infrared spectrum, which confirm there is no solvent present in the structure. The final 42.2 % product with the brown color is Mn_2O_3 (calcd: 42.0 wt %) and the small mass gain after 600 °C is presumably due to the oxidation of initial decomposed product Mn_3O_4 to Mn_2O_3 with further heating.[8]

Magnetism of 1: Powder magnetic characterization and heat capacity measurements support the classification of **1** as a homospin ferrimagnet.[9] In contrast to ferrimagnetism with uncompensated moments resulting from different cation valence states, as in Fe_3O_4 with Fe^{II} and Fe^{III}, here ferrimagnetism arises due to the crystal structure, which supports different exchange interactions between the three unique Mn^{II} sites. The 40 Oe zero-field-cooled (ZFC) and field-cooled (FC) temperature dependent magnetic susceptibility ($\chi_m = M/H$) and susceptibility-temperature product ($\chi_m T$) for a powder sample of **1** are shown in Figure 3a. The sharp increase in χ_m at low temperatures, far beyond that expected for a paramagnet, and the qualitative shape of $\chi_m T - T$, are typical of ferrimagnetic ordering. Based on the inflection point in the field-cooled $\chi_m - T$ at 40 Oe, a transition temperature of 2.4 K is defined. The temperature dependence of χ_m^{-1} (Figure S3 in the Supporting Information) is linear above the ordering temperature and a Curie–Weiss fit from 50 to 300 K results in $\theta = -20.7$ K and $C = 4.40$ emu mol^{-1} K. The C value corresponds to $\mu_{eff} = 5.93 \mu_B$, which agrees well with the spin-only value of $5.92 \mu_B$ for an isolated $S = 5/2$ Mn^{II} ion. The negative Weiss value indicates that magnetic interactions are primarily antiferromagnetic and, in combination with the sharp increase in magnetization at low temperatures, supports the assignment of ferrimagnetic order. The ZFC and FC curves are coincident at high temperatures, but diverge slightly below 3.0 K, indicating the presence of some form of hysteresis likely associated with the long-range magnetic order. The heat capacity displays a lambda anomaly at 2.3 K, reflecting the onset of long-range magnetic order (Figure 3b). A 1.9 K M-H sweep reveals that the molar magnetization saturates to $1.76\,N\beta$ at 50 kOe (Figure S4 in the Supporting Information). This is much smaller than the expected saturation value of $5\,N\beta$ for a spin-only Mn^{II} ion and is again consistent with ferrimagnetic order. A small M-H hysteresis loop with a coercivity of 10 Oe is observed, indicating that the ferrimagnetism of
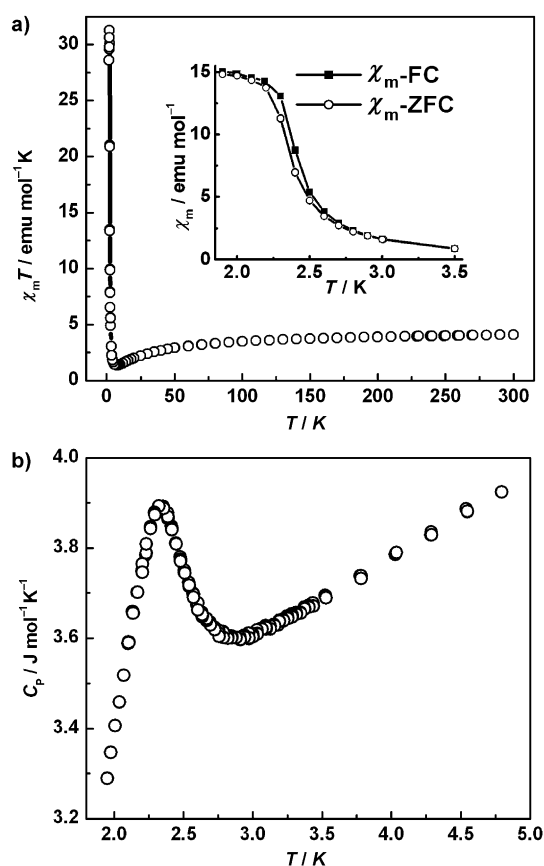

Figure 3. Powder magnetic measurements for **1**: a) Temperature dependent $\chi_m T$ plot at 40 Oe. Inset: FC/ZFC curves at low temperature. b) Heat capacity as a function of temperature in zero magnetic field.

compound **1** is relatively soft (Figure S4 in the Supporting Information).

To help elicit the magnetic structure of compound **1**, single-crystal magnetic measurements were performed in directions parallel and perpendicular to the c axis. χ_m as a function of T for both orientations and at different applied magnetic fields (100, 700, 900 Oe for $H \perp c$ and 20, 210, 700 Oe for $H//c$) is illustrated in Figure 4a. For low-field measurements along both orientations (100 Oe for $H \perp c$ and 20 Oe for $H//c$), the magnetization levels off below 2.5 K, consistent with the ferrimagnetic order of the system. For larger fields, the ordering transition broadens and we are unable to capture data at temperatures low enough to observe the magnetization leveling off. While it is well documented that antiferromagnetic interactions mediated by *syn–syn* and *syn–anti* carboxylates are relatively weak, we do not observe a spin-flop behavior along both orientations due to the decrease of susceptibility with increasing magnetic field.[10,11] The single crystal isothermal M-H sweeps at 1.9 K differ significantly from the bulk powder sample. As seen in the Figure 4b and S5 in the Supporting Information, the magnetizations for both orientations rise linearly at low magnetic fields and then increase more slowly at higher fields. The transition between the two regimes can be de-
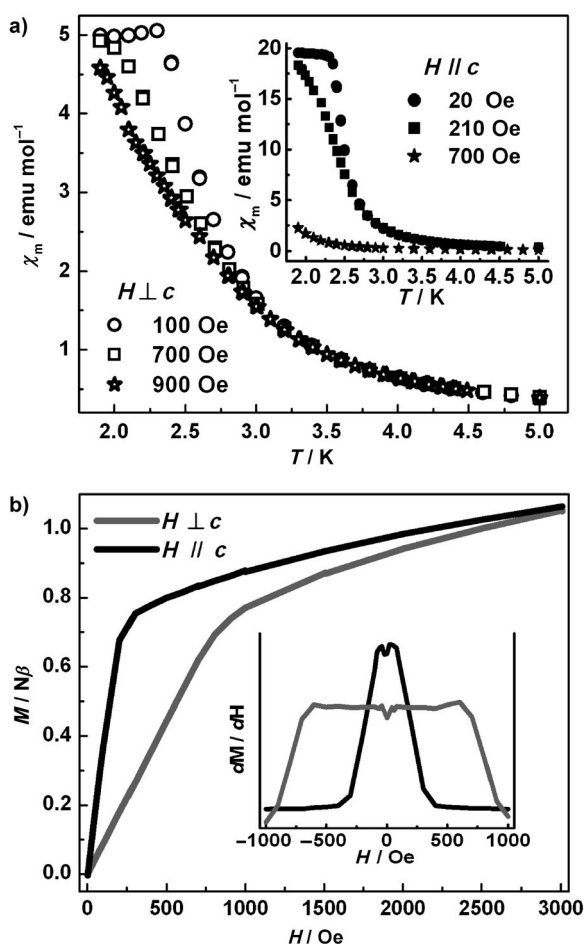
a)

b)

Figure 4. Single-crystal magnetic measurements of compound **1**: a) Temperature dependence of χ_m in different external fields ($H \perp c$: 100, 700, 900 Oe and $H//c$ (Inset) at 20, 210, 700 Oe). b) Field-dependent magnetizations and their derivatives at 1.9 K ($H \perp c$ and $H//c$).

fined by the inflection point, which yields transition fields of 100 Oe and 800 Oe for directions parallel and perpendicular to the *c* axis respectively. This behavior is due to significant magnetocrystalline anisotropy[10] which is a result of the layered structure of compound **1**. At high fields, the magnetization nearly saturates, reaching values of 1.73 Nβ and 1.88 Nβ at 50 kOe parallel and perpendicular to the *c* axis, respectively. While one may expect both directions saturate to the same value after all domains have been aligned, the smaller magnetization in the perpendicular direction may be due to its larger diamagnetic background from the sample holder, which becomes apparent at high fields or temperatures. However, these values do agree well with the 1.76 Nβ measured for the powder sample.

The magnetic behavior can be understood based on a magnetic structure that arises from the different exchange pathways in the framework. The most important superexchange interactions within the inorganic layer are Mn2-O4-Mn3 (97.17°) and Mn2-O2-Mn3 (99.87°) with a Mn2···Mn3 distance of 3.315 Å. Both could be antiferromagnetic, with the larger angle giving a slightly stronger antiferromagnetic

interaction.[12] As the ratio between the multiplicities of Mn2 and Mn3 atoms is 3 to 2, the proposed magnetic structure of the 2D layer is consequently ferrimagnetic with Mn2 atoms and Mn3 atoms pointing in opposite directions (Figure 5). These ferrimagnetic layers are connected to iso-
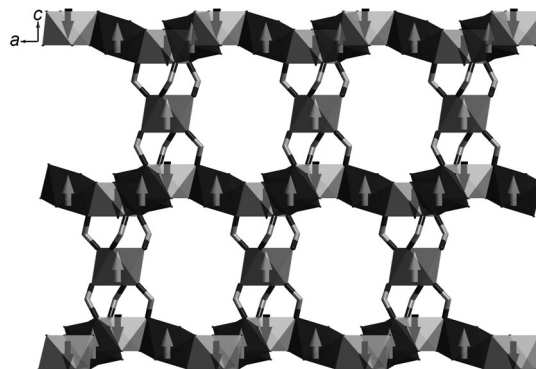

Figure 5. Proposed magnetic structure of **1**. Mn1O$_6$, Mn2O$_6$, and Mn3O$_6$ octahedra are presented by grey, black, and white, respectively (C2, C3, C4, C5A, C5B, C6A, and C6B are omitted for clarity).

lated Mn1O6 octahedra by *syn*, *anti–syn* carboxylates with nearest Mn3···Mn1 and Mn2···Mn1 distances of 4.065 and 5.879 Å respectively. In manganese coordination polymers, *syn–syn* and *syn–anti* carboxylates normally mediate weak antiferromagnetic coupling which is often suppressed by the application of a magnetic field.[11,13] As Mn3 is closest to Mn1, we expect them to point in opposite directions, and thus Mn2 and Mn1 will point in the same direction (Figure 5). Summing over the unit cell and accounting for site multiplicities, we then find the net saturation magnetization of the proposed magnetic structure to be 1.67 Nβ ({[(1/2-1/3)+1/6]×5Nβ}=1.67 Nβ), which agrees well with the value of 1.76 Nβ observed from the powder sample. The magnetic easy axis is parallel to the *c* axis because, as is shown in Figure 4, in this direction the low field susceptibility is larger and the transition field is smaller, as compared to measurements perpendicular to the *c* axis. Our hypothesis for the magnetic structure could be confirmed by low temperature neutron diffraction, though the low magnetic ordering temperature and need for deuteration both present significant experimental challenges.

Nanoindentation Studies: Turning to the nanoindentation studies, representative *P-h* curves obtained on the natural {003} and artificially polished {−230} facets of single crystals of compound **1** are shown in Figure 6a. The loading part of the *P-h* curves obtained on both facets is smooth, indicating that the plastic deformation, which occurs underneath the sharp indenter tip during indentation, is relatively homogeneous in nature. The average values of *H* and *E*, extracted from the *P-h* curves, are 0.89±0.05, 18.30±0.70 GPa for {003} and 1.22±0.06, 24.20±0.44 GPa on {−230}, respectively. This indicates that crystal properties are highly anisotropic with approximately 32% and 37% differences in *E* and
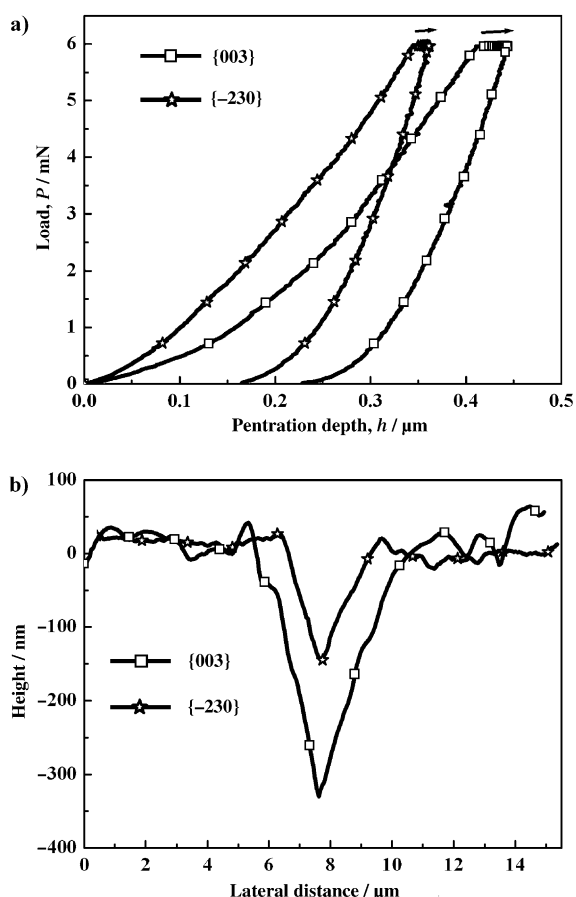
a)

b)

Figure 6. a) Representative *P-h* curves of compound **1** obtained from indentation normal to {003} and {−230} facets. b) Horizontal cross-section at the center of the residual indent impression on {003} and {−230} facets.

H, respectively. The AFM images of the residual impressions made on both of the facets are shown in Figure 7a and b. No 'pile-up' of material at the periphery of the indents could be found. The horizontal cross-sectional line profile at the middle of the indent for both facets shows that the residual penetration depth and the surface area of the impression from {003} are significantly higher than {−230}, as shown in Figure 6b.

a)

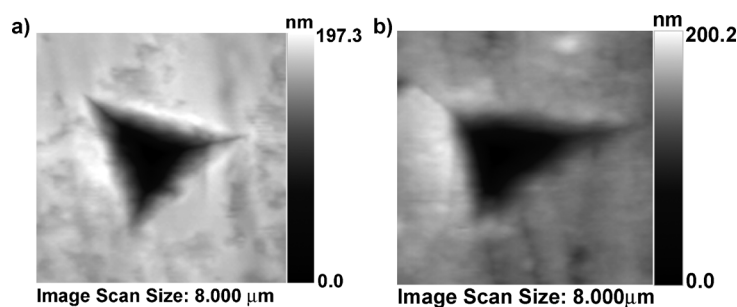Image Scan Size: 8.000 μm

b)

Image Scan Size: 8.000μm

Figure 7. AFM topographical images of indents: a) {003} face, b) {−230} face.

The anisotropy in mechanical properties of compound **1** can be rationalized with the aid of the underlying crystal structure. Though the loading during indentation is not perfectly uniaxial and the stress field generated underneath the indenter is non-uniform, indentation can be used to probe the anisotropy in the mechanical properties of single crystals because the measured modulus is strongly dependent on the elastic response along the indenter axis and is weakly affected by the transverse directions.[2,5a,b] In metals and semiconductors, plastic deformation is well understood in terms of the nucleation, rapid multiplication and propagation of dislocations. In amorphous materials, they arise due to shear bands.[14] However, it is believed that in organic and hybrid crystals, plastic deformation by slipping occurs along a specific crystallographic plane when sheets within the framework glide across one another, similar to a stack of playing cards in a deck.[5b,15]

As illustrated in Figure 1 and 2, the Mn2 and Mn3 atoms are linked by O2 and O4 atoms from both of the carboxylates of the 2-methylsuccinate ligands to form the manganese oxide layers along the *ab* plane. Such backbone structure imparts higher stiffness to the structure. These stiff layers are further connected by *anti, syn–syn* carboxylates with isolated $Mn1O_6$ octahedra to give rise to a 3D framework with an alternating linked-mode. For indentation on {003}, it can be seen from Figure 2b that the indenter axis is down *ab* plane, which is perpendicular to the stiff and planar inorganic layers. Thus, the deformation is likely associated with the isolated $Mn1O_6$ octahedra and their projecting *anti, syn–syn* carboxylates. Since the site multiplicity of Mn2 and Mn3 are of 1/2 and 1/3 in the asymmetric unit and exactly five times that of Mn1 site, the indentation load is carried by the edge-shared three $Mn2O_6$ octahedra and two $Mn3O_6$ octahedra within the layer instead of only one isolated $Mn1O_6$ octahedra. Thus, these isolated $Mn1O_6$ octahedra and their projecting carboxylates have to accommodate five times the stress as is passed by edge-shared Mn2 and Mn3 octahedra in the layer. This forces the $Mn1O_6$ octahedra and/or the projecting carboxylates to deform to some degree. Although the sp^2 hybridized carboxylates resist deformation as they cannot be easily stretched due to their high stretching vibration energy, they are susceptible to rotations. In addition, the isolated $Mn1O_6$ octahedra can also be deformed more easily than the stiff edge-shared inorganic manganese oxide layer because of the large separation between adjacent layers (ca. 12 Å), which allows for translational and torsional motions of isolated $Mn1O_6$ octahedra with comparatively low vibration energies. Further closer examination of the structure shows that the planes of these rigid *anti, syn–syn* carboxylates are not perpendicular to the *ab* plane but are at an angle of 68.1°. This can lead to motions of these carboxylates in order to accommodate the strain imposed by the indenter. Another factor to consider is that there are *a*/2 and *b*/2 length offsets along the *a* and *b* axes between adjacent layers. As a result, indentation of the {003} facet is not perpendicular to the $Mn1O_6$-carboxylates-2D layer-$Mn1O_6$ linkage, but is at an angle of 61.9°.

Hence, the $Mn1O_6$ octahedra or the *anti, syn–syn* carboxylates can shear relatively easily in comparison to a perfectly normal indentation. In contrast, when the {−230} facet is indented, the indenter axis (perpendicular to *ab* plane) is nearly parallel to the stiffest inorganic layers, leading to larger *H* and *E*.

Being of modest density (ca. 1.757 g cm$^{−3}$), the measured *E* and *H* values of compound **1** are relatively small in comparison to those reported for some dense hybrid crystals.[2,5a–c] However, compound **1** exhibits higher *E* and *H* values than porous hybrids.[5d–f, 16] In a hexagonal crystal system, the {001} planes are the favored planes for slip, as inferred from density functional theory.[17] Accordingly, slip is preferred along the *ab* plane. The AFM topographical image (Figure 7b) of the indentation impression on the {−230} facet shows cracking parallel to the inorganic layer. However, no cracks were observed in the other directions. These observations indicate that the rupture of linkages between the stiff inorganic layers and the isolated $Mn1O_6$ octahedra is the cause for the cracking.[5a]

Conclusion

We prepared a new 3D metal-organic framework [Mn(2-methylsuccinate)]$_n$ (**1**) and studied the structure by using X-ray single-crystal diffraction. The highly anisotropic structure comprises alternating manganese oxide layers and isolated MnO_6 octahedra, pillared *via syn*, *anti–syn* carboxylates. Powder magnetic characterization and heat capacity measurements indicated **1** is a homospin ferrimagnet. Detailed single-crystal magnetic study revealed the easy-axis and suggested a reasonable magnetic structure model. Nanoindentation on single-crystal showed anisotropic moduli and hardness parallel and perpendicular to the manganese oxide layer, which confirms the stiffness of the inorganic layers and the flexibility of the isolated MnO_6 octahedra with projecting carboxylates. Both sets of anisotropic properties arise from the unusual alternation of inorganic manganese oxide layers and isolated MnO_6 octahedra. This study presents clear evidence that unique structural features in the crystal can lead to both high magnetic and mechanical anisotropy, and thus encourages the use of crystal engineering and design to control and direct the anisotropic magnetic[1d,e] and mechanical[2, 18] properties of framework materials.

Experimental Section

General information: All chemicals and solvents were of reagent grade and used as received. Infrared spectra were collected over the range of 4000–500 cm$^{−1}$ on a Bruker Tensor-27 ATR spectrometer. Elemental analysis was obtained at the Department of Chemistry, the University of Cambridge (UK). Thermogravimetric analysis (TGA) was performed in air on a TA instruments Q50 using a heating rate of 10 °C minute$^{−1}$. Powder X-ray diffraction (PXRD) data were obtained using a Bruker D8 powder diffractometer with Cu$_{Kα}$ radiation.

Synthesis: (*R*)-2-Methylsuccinic acid (0.25 mmol, 0.033 g), NaOH (0.5 mmol, 0.020 g) and Mn(NO$_3$)$_2$·4H$_2$O (0.25 mmol, 0.085 g) were well mixed in a 20 mL vial with distilled water (5 mL). Then absolute ethanol (5 mL) was layered on the top of the solution and the vial was heated at 100 °C for 5 days and quenched in water to room temperature. Colorless platelet crystals of **1** were manually obtained in 26 % yield on the basis of manganese. FT-IR (KBr): $\tilde{v}$ = 2971 (w), 2931 (w), 1615 (m), 1579 (vs), 1437 (w), 1405 (vs), 1368 (m), 1316 (w), 1305 (m), 1255 (w), 1200 (w), 1121 (w), 1042 (w), 968 (w), 926 (w), 879 (w), 842 (w), 779 (w), 669 (m), 653 (m), 616 (w), 569 cm$^{−1}$ (m); elemental analysis calcd (%) for C$_5$H$_6$O$_4$Mn (185.04): C 32.45, H 3.27; found: C 32.28, H 3.29.

Single crystal X-ray crystallography study: Single-crystal X-ray diffraction data of compound **1** were collected on a Bruker-Nonius Kappa diffractometer equipped with a Bruker Apex II CCD detector using X-rays from a Bruker-Nonius FR591 rotating anode X-ray generator (Mo$_{Kα}$ radiation, $λ$ = 0.71073 Å). Data were collected over the range 2.91 to 27.48° (2$θ$) at 120 K by using a platelet crystal (0.18 × 0.14 × 0.08 mm^3). Absorption corrections were applied by using SADABS.[19] The structure was solved by direct methods and successive Fourier difference syntheses, and refined by full matrix least-squares procedure on F^2 with anisotropic thermal parameters for all non-hydrogen atoms using the programs SHELXS-97 and SHELXL-97 respectively.[20] Hydrogen atoms were not refined and the bond lengths between C2−C5A, C2−C5B, C3−C6A, and C3−C6B were constrained by using the DFIX commands due to the seriously disordered methyl group. X-Seed was used as an interface for the SHELX programs.[21] The crystallographic data are summarized in Table 1 and selected bond lengths and angles are listed in Table S1 in the Supporting Information. Single-crystal cell measurements of compound **1** were collected on an Oxford CCD diffractometer with graphite-monochromated Mo$_{Kα}$ radiation ($λ$ = 0.71073 Å) at 120 K. Data reduction, absorption corrections and face indexation were applied and determined using the CrysAlis^{Pro} program.[22] CCDC-821841 contains the supplementary crystallographic data for this paper. These data can be obtained free of charge from The Cambridge Crystallographic Data Centre via www.ccdc.cam.ac.uk/data_request/cif.

Magnetic measurements on powder and single crystals: The temperature and field dependence of the dc magnetization was measured with a Quantum Design MPMS 5XL SQUID magnetometer. Powder samples were well-ground, contained in gel caps, and held in a straw with a uniform diamagnetic background. Single crystals were measured in two unique crystallographic directions. For measurements in the *ab* plane, the platelet was placed flat along the straw and held in place by Kapton tape. The platelet was laid flat in the bottom of a gel cap for measurements perpendicular to the *c* axis.

Powder heat capacity measurements: Heat capacity measurements were performed using the semi-adiabatic technique, as implemented in a Quantum Design Physical Property Measurement System (PPMS). To improve thermal coupling, a small amount of Apiezon N grease was placed between the sample and stage. Samples were also mixed and ground with equal masses of Ag powder and pressed into pellets in order to increase thermal conductivity. The contributions from the grease and Ag were measured separately and subtracted.

Nanoindentation methodology on single crystals: Since the platelet crystal does not have any natural facet perpendicular to the major facet {003}, we had to polish off a certain natural facet to get an artificial facet {−230} which is almost perfectly perpendicular to the major facet {003}. Accordingly, the nanoindentation experiments were performed on the {003} and artificially polished {−230} facets using a nanoindenter (Triboindenter of Hysitron, Minneapolis, USA) with an in-situ imaging capability. The machine continuously monitors and records the load (*P*) and displacement (*h*) of the indenter with force and displacement resolutions of 1 nN and 0.2 nm, respectively. A Berkovich diamond indenter with a tip radius of about 100 nm was used to indent the crystals. In order to identify flat regions for the experiment, the crystal surfaces were imaged prior to indentation using the same indenter tip. A loading and unloading rate of 0.6 mN s$^{−1}$ and a hold time of 30 s at peak load were employed. A minimum of 10 indentations were performed on each crystallographic facet. The indentation impressions were captured immediately after un-

FULL PAPER

loading, so as to avoid time-dependent elastic recovery of the residual impression. The experiments were conducted using quasi-static (load-controlled) mode. Contact stiffness, S is determined from the slope of the load-displacement (P-h) curve at the initial point of unload (i.e., $S = dP/dh$), therefore E and H can be found only at the maximum indentation depth. The elastic contact stiffness determined from the P-h curves is later used to calculate the reduced modulus, E_r, according to Equation (1):[23]

$$E_r = \frac{\sqrt{\pi}}{2\beta} \frac{S}{\sqrt{A_c}} \tag{1}$$

where A_c is the contact area under load (based on the calibrated tip areal function) and β is a constant that depends on the geometry of the indenter ($\beta = 1.034$ for a Berkovich tip). The method proposed by Oliver and Pharr ()[24] to extract the sample elastic modulus from the reduced modulus assumes isotropic elastic properties, which is normally not the case for single crystals. To account for the effects of anisotropy in single crystals, it has been shown[23a, 25] that the modulus obtained from nanoindentation of a single crystal is more appropriately represented as an "indentation modulus", given by Equation (2):

$$\frac{1}{E} = \frac{1 - v_i^2}{E_i} + \frac{1 - v_s^2}{E_s} \tag{2}$$

where v and E are Poisson's ratio and elastic modulus, respectively; and the subscripts i and s refer to the indenter and test material, respectively. The indenter properties used in this study are $E_i = 1141$ GPa, and Poisson's ratio for the indenter is $v_i = 0.07$. The hardness of a material is defined as its resistance to local plastic deformation. Thus, indentation hardness, H, can be determined from the maximum indentation load, P_{max}, divided by the contact area, A [Eq. (3)]:

$$H = \frac{P_{max}}{A} \tag{3}$$

where the contact area (A) is a function of the contact depth, h_c, and can be determined by the Equation (4):

$$A(h_c) = C_0 h_c^2 + C_1 h_c + C_2 h_c^{1/2} + C_3 h_c^{1/4} + \dots\dots + C_8 h_c^{1/128} \tag{4}$$

It may be noted that only the constant C_0 is used, if it is assumed that a Berkovich indenter has a perfect tip. However, for imperfect tips, higher-order terms have to be taken into account and these are obtained from the tip-area function curve fit for a given tip.

The contact depth can be estimated from the load-displacement data using Equation (5):

$$h_c = h_{max} - \varepsilon \frac{P_{max}}{S} \tag{5}$$

where h_{max} is the maximum indentation depth and 0.75 (P/S) denotes the extent of elastic recovery (h_e).

Acknowledgements

[1] a) A. K. Cheetham, C. N. R. Rao, R. K. Feller, *Chem. Commun.* **2006**, 4780–4795; b) A. K. Cheetham, C. N. R. Rao, *Science* **2007**, *318*, 58–59; c) C. N. R. Rao, A. K. Cheetham, A. Thirumurugan, *J. Phys. Condens. Matter* **2008**, *20*, 083202; d) M. Kurmoo, *Chem. Soc. Rev.* **2009**, *38*, 1353–1379; e) M. Nakano, H. Oshio, *Chem. Soc. Rev.* **2011**, *40*, 3239–3248; f) J. S. Miller, *Chem. Soc. Rev.* **2011**, *40*, 3266–3296; g) D.-F. Weng, Z.-M. Wang, S. Gao, *Chem. Soc. Rev.* **2011**, *40*, 3157–3181; h) W. Zhang, H.-Y. Ye, R.-G. Xiong, *Coord. Chem. Rev.* **2009**, *253*, 2980–2997; i) T. Hang, W. Zhang, H.-Y. Ye, R.-G. Xiong, *Chem. Soc. Rev.* **2011**, *40*, 3577-3598; j) Z.-M. Wang, K. Hu, S. Gao, H. Kobayashi, *Adv. Mater.* **2010**, *22*, 1526–1533.

[2] J. C. Tan, A. K. Cheetham, *Chem. Soc. Rev.* **2011**, *40*, 1059–1080.

[3] a) X.-Y. Wang, L. Wang, Z.-M. Wang, G. Su, S. Gao, *Chem. Mater.* **2005**, *17*, 6369–6380; b) M. Kurmoo, H. Kumagai, S. M. Hughes, C. J. Kepert, *Inorg. Chem.* **2003**, *42*, 6709–6722; c) W.-X. Zhang, W. Xue, Y.-Z. Zheng, X.-M. Chen, *Chem. Commun.* **2009**, 3804–3806.

[4] a) W. Zhang, Y. Cai, R.-G. Xiong, H. Yoshikawa, K. Awaga, *Angew. Chem.* **2010**, *122*, 6758–6760; *Angew. Chem. Int. Ed.* **2010**, *49*, 6608–6610; b) H.-B. Cui, K. Takahashi, Y. Okano, H. Kobayashi, Z.-M. Wang, A. Kobayashi, *Angew. Chem.* **2005**, *117*, 6666–6670; *Angew. Chem. Int. Ed.* **2005**, *44*, 6508–6512; c) H. Cui, Z.-M. Wang, K. Takahashi, Y. Okano, H. Kobayashi, A. Kobayashi, *J. Am. Chem. Soc.* **2006**, *128*, 15074–15075.

[5] a) J. C. Tan, J. D. Furman, A. K. Cheetham, *J. Am. Chem. Soc.* **2009**, *131*, 14252–14254; b) J. C. Tan, J. B. Orton, C. A. Merrill, A. K. Cheetham, *Acta Mater.* **2009**, *57*, 3481–3496; c) M. Kosa, J. C. Tan, C. A. Merrill, M. Krack, A. K. Cheetham, M. Parrinello, *ChemPhysChem* **2010**, *11*, 2332–2336; d) J. C. Tan, T. D. Bennett, A. K. Cheetham, *Proc. Natl. Acad. Sci. USA* **2010**, *107*, 9938–9943; e) T. D. Bennett, J. C. Tan, S. A. Moggach, R. Galvelis, M. D. Caroline, B. A. Reisner, A. Thirumurugan, D. R. Allan, A. K. Cheetham, *Chem. Eur. J.* **2010**, *16*, 10684–10690; f) T. D. Bennett, A. L. Goodwin, M. T. Dove, D. A. Keen, M. G. Tucker, E. R. Barney, A. K. Soper, E. G. Bithell, J. C. Tan, A. K. Cheetham, *Phys. Rev. Lett.* **2010**, *104*, 115 503.

[6] a) R. Vaidhyanathan, S. Natarajan, C. N. R. Rao, *Dalton Trans.* **2003**, 1459–1464; b) Z. Hulvey, A. K. Cheetham, *Solid State Sci.* **2007**, *9*, 137–143; c) Y. Kim, D.-Y. Jung, K.-P. Hong, G. Demazeau, *Solid State Sci.* **2001**, *3*, 837–846.

[7] D. N. Dybtsev, H. Chun, S. H. Soon, D. Kim, K. Kim, *J. Am. Chem. Soc.* **2004**, *126*, 32–33.

[8] P. J. Saines, B. C. Melot, R. Seshadri, A. K. Cheetham, *Chem. Eur. J.* **2010**, *16*, 7579–7585.

[9] a) Z. Wang, B. Zhang, H. Fujiwara, H. Kobayashi, M. Kurmoo, *Chem. Commun.* **2004**, 416–417; b) M.-H. Zeng, M.-C. Wu, H. Liang, Y.-L. Zhou, X.-M. Chen, S.-W. Ng, *Inorg. Chem.* **2007**, *46*, 7241–7243; c) J.-P. Zhao, B.-W. Hu, Q. Yang, T.-L. Hu, X.-H. Bu, *Inorg. Chem.* **2009**, *48*, 7111–7116; d) M.-H. Zeng, Y.-L. Zhou, M.-C. Wu, H.-L. Sun, M. Du, *Inorg. Chem.* **2010**, *49*, 6436–6442; e) N. Snejko, E. Gutiérrez-Puebla, J. L. Martínez, M. A. Monge, C. Ruiz-Valero, *Chem. Mater.* **2002**, *14*, 1879–1883; f) X.-M. Zhang, X.-H. Zhang, H.-S. Hu, M.-L. Tong, S. W. Ng, *Inorg. Chem.* **2008**, *47*, 7462–7464; g) J.-R. Li, Q. Yu, E. C. Sañudo, Y. Tao, W.-C. Song, X.-H. Bu, *Chem. Mater.* **2008**, *20*, 1218–1220.

[10] a) R. L. Carlin, *Acc. Chem. Res.* **1976**, *9*, 67–74; b) R. L. Carlin, A. J. van Duyneveldt, *Acc. Chem. Res.* **1980**, *13*, 231–236.

[11] a) X.-Y. Wang, Z.-M. Wang, S. Gao, *Chem. Commun.* **2007**, 1127–1129; b) W. Li, H.-P. Jia, Z.-F. Ju, J. Zhang, *Dalton Trans.* **2008**, 5350–5357; c) W. Li, P. T. Barton, R. P. Burwood, A. K. Cheetham, *Dalton Trans.* **2011**, *40*, 7147–7152.

[12] a) M. J. Plater, M. R. St J. Foreman, R. A. Howie, J. M. S. Skakle, E. Coronado, C. J. Gómez-García, T. Gelbrich, M. B. Hursthouse, *Inorg. Chim. Acta* **2001**, *319*, 159–175; b) T. Yamase, K. Fukaya, H. Nojiri, Y. Ohshima, *Inorg. Chem.* **2006**, *45*, 7698–7704.

[13] T. K. Maji, S. Sain, G. Mostafa, T. H. Lu, J. Ribas, M. Monfort, N. R. Chaudhuri, *Inorg. Chem.* **2003**, *42*, 709–716.

[14] a) P. Murali, U. Ramamurty, *Acta Mater.* **2005**, *53*, 1467–1478; b) B. Viswanath, R. Raghavan, U. Ramamurty, N. Ravishankar, *Scr.*

Mater. **2007**, *57*, 361–364; c) N. Gane, *Proc. R. Soc. London. Ser. A* **1970**, *317*, 367–391.

[15] a) C. M. Reddy, R. C. Gundakaram, S. Basavoju, M. T. Kirchner, K. A. Padmanabhan, G. R. Desiraju, *Chem. Commun.* **2005**, 3945–3947; b) M. S. R. N. Kiran, S. Varughese, C. M. Reddy, U. Ramamurty, G. R. Desiraju, *Cryst. Growth Des.* **2010**, *10*, 4650–4655.

[16] D. F. Bahr, J. A. Reid, W. M. Mook, C. A. Bauer, R. Stumpf, A. J. Skulan, N. R. Moody, B. A. Simmons, M. M. Shindel, M. D. Allendorf, *Phys. Rev. B* **2007**, *76*, 184106.

[17] M. Hebbache, *Solid State Commun.* **2000**, *113*, 427–432.

[18] C. M. Reddy, G. R. Krishna, S. Ghosh, *CrystEngComm* **2010**, *12*, 2296–2314.

[19] G. M. Sheldrick, SADABS, 2007/2, Bruker AXS Inc., Madison, Wisconsin, **2007**.

[20] G. M. Sheldrick, *Acta Crystallogr. Sect. A* **2008**, *64*, 112–122.

[21] L. J. Barbour, *J. Supramol. Chem.* **2001**, *1*, 189–191.

[22] *CrysAlisPro*, Oxford Diffraction, Version 1.171.34.34.

[23] a) E. T. Lilleodden, J. A. Zimmerman, S. M. Foiles, W. D. Nix, *J. Mech. Phys. Solids* **2003**, *51*, 901–920; b) P. Kumar, M. S. R. N. Kiran, *Nanoscale Res. Lett.* **2010**, *5*, 1085–1092.

[24] a) W. C. Oliver and G. M. Pharr, *J. Mater. Res.* **1992**, *7*, 1564–1583; b) W. C. Oliver, G. M. Pharr, *J. Mater. Res.* **2004**, *19*, 3–21.

[25] a) J. J. Vlassak, W. D. Nix, *J. Mech. Phys. Solids* **1994**, *42*, 1223–1245; b) H. Bei, E. P. George, G. M. Pharr, *Scr. Mater.* **2004**, *51*, 875–879; c) A. C. F. Cripps, *Introduction to Contact Mechanics*, 2nd ed., Springer, New South Wales, Australia, **2007**, Chapter 12, p. 214.